Article

Synthesis and Characterization of NiCoPt/CNFs Nanoparticles as an Effective Electrocatalyst for Energy Applications

Esam E. Abdel-Hady [1,2], Mohamed Shaban [3,4,*], Mohamed O. Abdel-Hamed [1,2], Ahmed Gamal [4], Heba Yehia [1] and Ashour M. Ahmed [4]

1   Physics Department, Faculty of Science, Minia University, Minia 61519, Egypt;
    esamhady@yahoo.com (E.E.A.-H.); mazosman2005@yahoo.com (M.O.A.-H.); hdody393@gmail.com (H.Y.)
2   Academy of Scientific Research and Technology (ASRT) of the Arab Republic of Egypt, Cairo 11516, Egypt
3   Department of Physics, Faculty of Science, Islamic University in Madinah,
    Al-Madinah Al-Munawarah 42351, Saudi Arabia
4   Nanophotonics and Applications (NPA) Lab, Physics Department, Faculty of Science, Beni-Suef University,
    Beni-Suef 62514, Egypt; a_gamal21@yahoo.com (A.G.); ashour.elshemey@gmail.com (A.M.A.)
*   Correspondence: mssfadel@aucegypt.edu

Abstract: In this work, three nanoparticle samples, $Ni_4Co_2Pt/CNFs$, $Ni_5CoPt/CNFs$ and $Ni_6Pt/CNFs$, were designed according to the molar ratio during loading on carbon nanofibers (CNFs) using electrospinning and carbonization at 900 °C for 7 h in an argon atmosphere. The metal loading and carbon ratio were fixed at 20 and 80 wt%, respectively. Various analysis tools were used to investigate the chemical composition, structural, morphological, and electrochemical (EC) properties. For samples with varying Co%, the carbonization process reduces the fiber diameter of the obtained electrospun nanofibers from 200–580 nm to 150–200 nm. The EDX mapping revealed that nickel, platinum, and cobalt were evenly and uniformly incorporated into the carbonized PVANFs. The prepared Ni-Co-Pt/CNFs have a face-centered cubic (FCC) structure with slightly increased crystallite size as the Co% decreased. The electrocatalytic properties of the samples were investigated for ethanol, methanol and urea electrooxidation. Using cyclic voltammetry (CV), chronoamperometry, and electrochemical impedance measurements, the catalytic performance and electrode stability were investigated as a function of electrolyte concentration, scan rate, and reaction time. When Co is added to Ni, the activation energy required for the electrooxidation reaction decreases and the electrode stability increases. In 1.5 M methanol, the $Ni_5CoPt/CNFs$ electrode showed the lowest onset potential and the highest current density (30.6 A/g). This current density is reduced to 28.2 and 21.2 A/g for 1.5 M ethanol and 0.33 M urea, respectively. The electrooxidation of ethanol, methanol, and urea using our electrocatalysts is a combination of kinetic/diffusion control limiting reactions. This research provided a unique approach to developing an efficient Ni-Co-Pt-based electrooxidation catalyst for ethanol, methanol and urea.

Keywords: Ni-Co-Pt/CNFs; electrocatalyst; ethanol; methanol; urea; electrooxidation; impedance spectroscopy

1. Introduction

Energy is a crucial factor that affects both economic progress and human survival. Concerns about human health and environmental hazards have grown significantly in recent decades. Many of these problems, such as acid rain, ozone depletion, and global climate change, are related to energy production, transformation, and consumption. Today, energy supplies are running out, prompting a greater desire to find clean renewable alternative fuels. Polymer-electrolyte membrane fuel cells (PEMFCs) are a potential solution for producing clean energy. PEMFCs have received a lot of attention due to their high efficiency, high power density, ease of scale-up, and low operating temperatures [1]. However, the high cost of Pt catalysts, combined with limited resources, has sparked interest in

developing free or low-content platinum group metal catalysts for use in PEMFCs [2]. As a result, the following two strategies are being used to reduce Pt usage. The first is to reduce the size of the catalyst particles, resulting in a higher specific surface area. At the nanoscale, size has been found to influence catalytic properties, whereas NPs in the 1–30 nm range exhibit better catalytic efficacy as size decreases [3]. Also, the crystallographic growth plane of the catalyst was found to have an impact on the catalytic property. For example, the reaction rate on Pt {111} was found to be roughly five times that of the {100} plane in the dehydrogenating cyclization process of n-butane [4]. The second strategy is to combine Pt with less expensive elements with moderate catalytic activity, such as Co, Ni, Fe, and others [5–10].

Noble metallic nanoparticles (NPs) and carbon-based materials of various sizes, shapes, facets, and compositions are widely used in the catalytic industries because of their distinct properties [11–20]. For example, Pt is used in automobiles to convert harmful exhaust gases such as CO, NOx, and hydrocarbons into CO_2, N_2 and H_2O. Also, Pt is widely employed as a catalyst in the fuel cell, however, the lethargic oxygen reduction (OR) and its slow kinetics on Pt being claimed to limit the operation of the fuel cells [21–25]. Many groups have recently conducted several studies to improve Pt catalysts' performance in the negative electrode, including their activity and stability [11,12]. Different cathodic catalysts based on Pt alloys have been developed such as Pt/Fe, Pt/Co, Pt/Ni, and Pt/Cr [26–32]. These catalysts have been employed in PEMFCs for hydrogen oxidizing at the anode and the oxygen reduction occurs at the cathode due to the low overpotential and strong catalytic activity [26]. Also, Pt is alloyed with 3d transition metal to achieve high activity at 0.9 $V_{iR-free}$ for the oxygen-reducing reaction (ORR) [28,33–38]. Compared to pure Pt in PEMFCs, Pt-alloys containing different transition metals, such as Ni, Cr, Co, and others, have shown increased ORR electrocatalytic activities [29,36–39]. This improvement can be attributed to a variety of factors, including a decrease or reduction in the Pt oxidation state, suppression of Pt oxide formation, formation of new electronic structures with increased Pt 5d orbital vacancies, improvement of O_2 adsorption due to the decrease in the Pt-Pt interatomic distance, formation of a thin Pt skin on the alloy core surfaces, and modified electronic structure of the highest-ranked Pt atoms [34,36,37,40–46].

The PtCo catalyst has gained a lot of attention amongst Pt-alloy catalysts because of its high stability and activity in acidic environments [29,47]. Paulus et al. looked at bulk Pt compositions of 50 and 75 percent Pt with Ni and Co alloying components [35,48]. The 25 at. percent Ni and Co catalysts showed a small activity rise of around 1.5 times, while the 50 at. percent Ni and Co catalysts showed a more substantial enhancement of factor 2–3 when compared to pure Pt. For the ORR, Huang et al. found that PtCo alloy nanoparticles have activity and specific activity improvements of 1.3–3.2 and 1.2–2.2, respectively, when compared to pure Pt [49]. Antolini et al. found that PtCr and PtCo are significantly more stable in terms of catalytic activity and stability than PtV, PtNi and PtFe due to their high degree of alloying and particle size [29]. Jayasayee et al. investigated the activity and durability of PtCo, PtNi and PtCu in PEMFC cathodes as a function of alloying elements [38]. Relative to PtNi and Pt electrocatalysts, the performances of PtCo and PtCu electrocatalysts were observed to be the most appealing. The activities of PtCu, PtCo and PtNi alloys in PEMFCs were examined by Mani et al. [39]. Pt-alloys containing Co and Cu were shown to be more active than PtNi. Relative to the commercial Pt/C electrocatalyst, the masses and specific activities of PtCo and PtCu were increased by a ratio of 3–4.

Although these attempts, the commercialization of Pt-based PEMFCs for several applications; including portable electronics, automotive, and stationary electricity; is still required higher durability, lower cost, and higher efficiency than the existing levels. Also, commercial fuel cell lifetime requirements vary greatly depending on the application: 5000 h for vehicles, 20,000 h for buses, and 40,000 h for immobile applications [33]. So, the development of morphologically and structurally managed Pt nanostructures or innovative Pt-based nanocomposites is urgently required to meet the ever-increasing demand in energy and related fields.

In this work, we suggest the design of a particulate nanocomposite from Ni and Co with a limited ratio of Pt (3%) and the use of a low-cost supporting nanofibrous for the mass production of a low-cost nano electrocatalyst toward the design of commercial fuel cells. This work aims to fabricate and characterize a low-cost electrocatalyst utilizing Co and Ni as replacements of the Pt. Here, NiCoPt/CNFs nanoparticles-incorporated carbon nanofibers are designed, characterized, and investigated as electrocatalysts for electrooxidation of ethanol, methanol, and urea. The influence of the Ni/Co ratio on electrocatalyst morphologies, structures, and electrooxidation performance was examined. The electrocatalysts are characterized by X-ray diffraction (XRD), energy dispersive X-ray mapping (EDX), transmission electron microscopy (TEM), and scanning electron microscopy (SEM). The electrocatalytic properties of the samples are studied for electrooxidation of ethanol, methanol, and urea in an alkaline medium. The effects of electrolyte concentration, scan rate, and reaction duration on the performance of the proposed catalysts are investigated. Furthermore, the electrode stability and performance are examined using cyclic voltammetry (CV), chronoamperometry, and electrochemical impedance spectroscopy (EIS) measurements. The Ni-Co-Pt ternary nanoparticles are likely to be useful as a free catalyst in fuel cell applications.

2. Experimental Details

2.1. Samples Preparation

Figure 1 shows a schematic illustration of the synthetic procedure of metal embedded in carbon nanofibers (MNPs/CNFS). Solutions of PVA (Alpha, Germany) 10 wt% concentration in water containing Nickel (II) acetate tetrahydrate (NiAc, 98% (Alpha, Germany)), Cobalt acetate (CoAc, 98% (Alpha, Germany)), and H_2PtCl_6 (Alpha, Germany). The theoretical metal loading and carbon ratio were fixed at 20 and 80 wt%, respectively. The theoretical Ni:Co:Pt molar ratio is 55:30:15, 70:15:15 and 85:15 for $Ni_4Co_2Pt/CNFs$, $Ni_5CoPt/CNFs$ and $Ni_6Pt/CNFs$, respectively. Typically, 1.2896:1.9930 gm NiAc ($Ni_{11:17wt\%}$), 0.25–0.5 gm CoAc ($Co_{3-6wt\%}$) and 0.1755 gm H_2PtCl_6 ($Pt_{3wt\%}$) were mixed with PVA solution to make a combination of 80 weight percent polymer and 20 weight percent (Ni/Co/Pt) of various mass ratios. For all samples, total metal loading was kept at 20%, with varying percentages of particular metals as shown in Table 1. The mixture was stirred at room temperature (RT) overnight until it obtained a clear and homogeneous solution. Homogeneous electrospinning solutions were loaded in 20 mL. Positive voltage, working distance, and flow rate were the optimal Electrospinning parameters, which were 22 kV, 15 cm and 0.3 mL/h, respectively. On the surface of a metal plate, nanofibers were accumulated as a fibrous web. The electrospun PVA/Ni(Ac)-Co(Ac)-H_2PtCl_6 nanofibers were dried in a vacuum at 80 °C for 24 h before being carbonized in an argon environment at 900 °C for 7 h (heating rate 3 °C/min, holding 2 h).

Table 1. Metal composition of the electro-catalysts in total metal loading of 20 wt%.

Catalyst Name	Catalyst Molar Ratio	Ni, wt%	Co, wt%	Pt, wt%	Metal wt%
S1	$Ni_4Co_2Pt/CNFs$	11	6	3	20
S2	$Ni_5CoPt/CNFs$	14	3	3	20
S3	$Ni_6Pt/CNFs$	17	0	3	20

2.2. Samples Characterization

A scanning electron microscope (SEM) (Jeol JSM-I T 200, Tokyo, Japan) equipped with energy dispersive X-rays (EDX) was used to examine the surface morphology of the nanofibers. Using an X-ray diffractometer (202964/Panalytical Empryan, Malvern, UK) and Cu K_α ($\lambda = 0.1540$ Å) radiation, the structure and crystallinity of the produced catalyst were investigated. The diffraction pattern was investigated over a range from 10° to 100° at a step size of 0.05. An electrochemical analyzer (CHI 660E Series, Austin, TX, USA) was used

to measure the electrocatalytic activities of electrodes as anode or cathode for methanol or ethanol electro-oxidation. The electrochemical cell consisted of three electrodes: a reference electrode (Ag/AgCl; KCl solution concentration was 4.0 M), an auxiliary (counter) electrode (Pt wire), and the working electrode (Ag/AgCl) (glassy carbon electrode; GC).
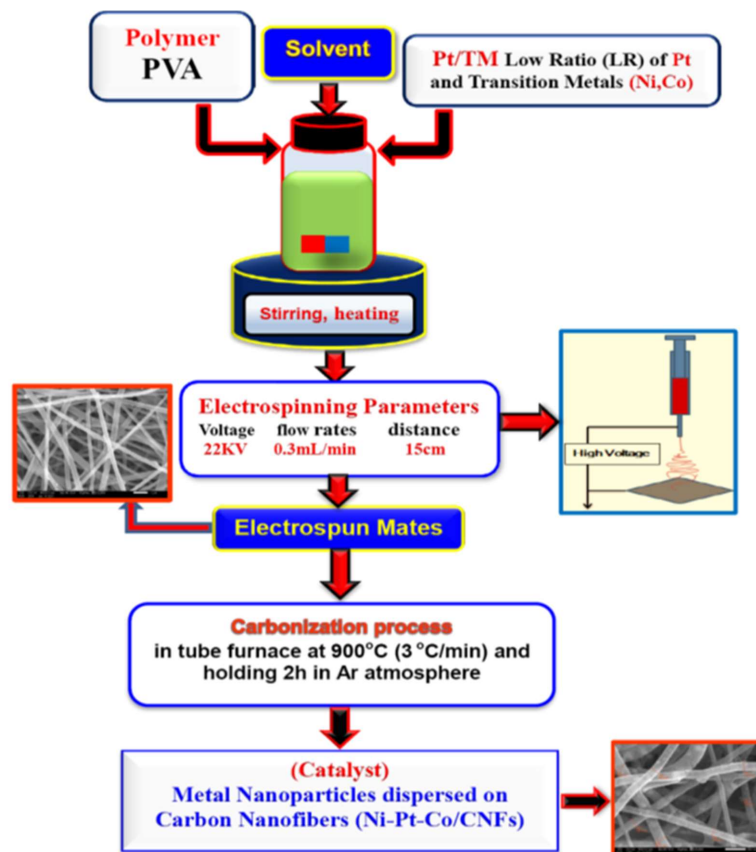
Figure 1. Schematic illustration of the synthetic procedure of Metal embedded in Carbon Nanofibers (MNPs/CNFS).

2.3. Electrochemical (EC) Measurements

The electrochemical analysis was performed in a typical three-electrode cell utilizing an electrochemical analyzer (CHI 660E Series, Austin, TX, USA). The experimental set-up and all its components were shown in Figure S1 (supplementary data).

The working electrodes were made in the following manner: In a tiny agate mortar, 5 mg of catalyst powder and 50 μL Nafion were disseminated in 0.4 mL Isopropyl alcohol and then crushed into a slurry. To make a homogenous catalyst ink, the mixture was stirred for 12 h. A slurry of around 16 μL was then applied directly to a glassy carbon electrode of 0.07065 cm^2 surface area. The electrode was then dried for 1 h at RT. Pt wire was used for the counter electrode, while Ag/AgCl was used for the reference electrode. As demonstrated in the figures for the Mott-Schottky curves, the potential was scanned from −0.2 to 0.8 V (versus Ag/AgCl) at various scan rates in different concentrations of solutions (Methanol, Ethanol, Urea). Electrochemical impedance spectroscopy (EIS) graphs with a frequency range of 100 kHz to 10 Hz and modulation amplitude of 5 mV were taken for these concentration measurements at an open circuit voltage (0.5 V vs. Ag/AgCl). Polarization curves obtained using linear sweep voltammetry (LSV) at RT with a 10 mV/s scan rate were used to assess the electrocatalytic activity of the samples.

3. Results and Discussion

3.1. Morphological Study

The electrospinning process was used to successfully produce PVA/NiAc-CoAc-Ptcl nanofibers. Figure 2A–C shows SEM images for the PVA nanofibers mats loaded with the salts of the metals (NiAc-CoAc-PtCl) before carbonization. All of the SEM images of the nanofibers obtained indicate clearly smooth, bead-free nanofibers. The average fiber diameter ranges from 200 to 580 nm. No significant difference was observed between the fiber morphologies of the prepared nanofibers. After the carbonization process, the polymer is transformed into carbon nanofibers [50], with metallic nanoparticles being distributed over them. Figure 2D–F shows SEM images of carbon nanofibers loaded with Ni_4Co_2Pt, Ni_5CoPt, and Ni_6Pt nanoparticles after carbonization at 900 °C in an argon atmosphere. These images demonstrate that the used approach for making decorated carbon nanofibers with metallic nanoparticles can be employed successfully. Except for reducing the fiber diameter to the range of 150–200 nm, the carbonization procedure had no significant influence on the nanofibrous shape of the electrospun nanofibers, as shown in the figure.
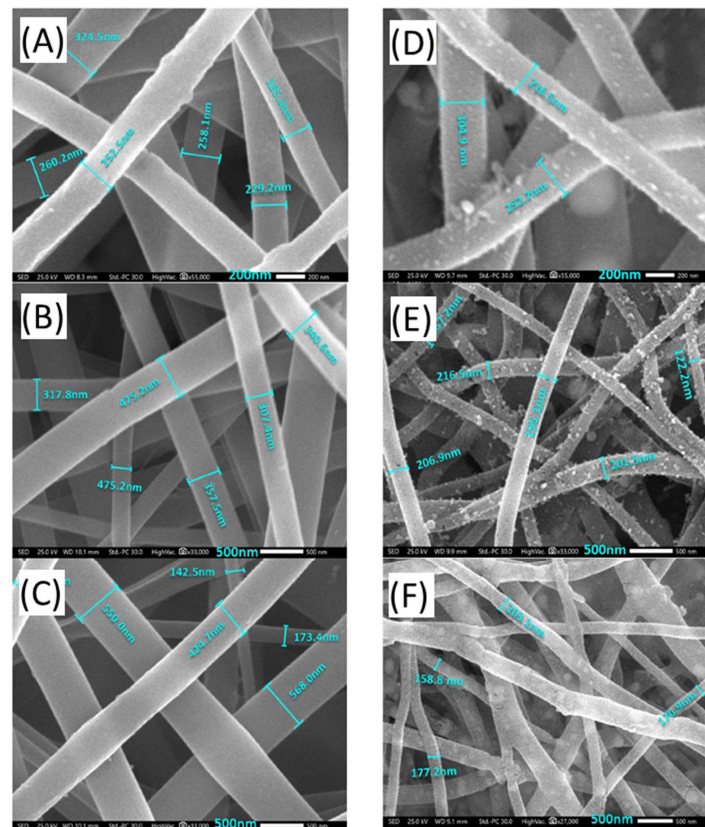
Figure 2. SEM images for (**A–C**) PVA/NiAc/CoAc/H_2PtCl_6 nanofibers mats before carbonization and (**D–F**) carbon nanofibers loaded with Ni_4Co_2Pt, Ni_5CoPt and Ni_6Pt nanoparticles (after carbonization).

The size and distribution of the metallic nanoparticles on the carbon nanofibers can be examined using a transmission electron microscope (TEM). Figure 3 shows TEM images with different magnifications for the sample S2 (Ni_5CoPt/CNFs), as an example. These TEM images demonstrated that the Ni_5CoPt NPs were almost homogeneously dispersed in the CNFs and evenly grown on the surface of CNFs. The inset of Figure 3A shows the nanoparticle diameter distribution. The average diameter of the NPs was ~23 nm.
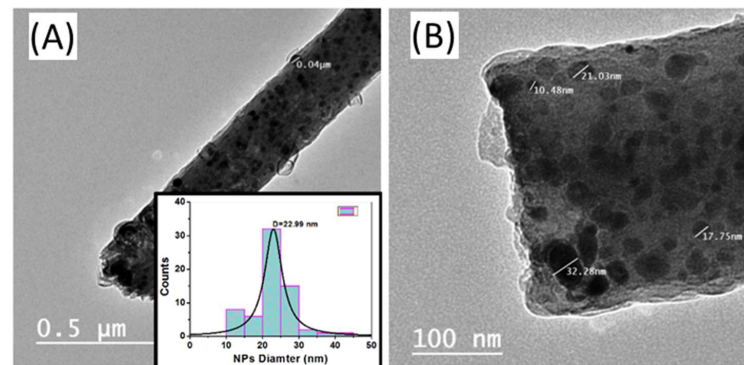
Figure 3. (**A**,**B**) TEM images with different magnifications for the sample $Ni_5CoPt/CNFs$. The inset in (**A**) shows the corresponding particle diameter distribution of Ni_5CoPt NPs on the surface of the CNFs.

3.2. Elemental Analysis

Figure 4 demonstrates the SEM image and corresponding EDX mapping analysis of the $Ni_4Co_2Pt/CNFs$ (sample 1) and $Ni_5CoPt/CNFs$ (sample 2), respectively. (IMG1) represents the area that was scanned to know the components of the fibers. From Figure 4, for sample 1 and sample 2, it can be seen that the distribution of C element as nanofibers was homogeneous and dense on the whole samples. Also, the nanoparticles of Ni, Pt and Co are distributed fully and uniformly on the surface of carbon nanofibers, as presented in the figure. Furthermore, the elemental mapping images (Figure 4) confirmed the shiny NPs as Ni, Pt and Co no other foreign impurities were detected, and this was also proven by the X-ray results. According to this study, transition metals (nickel, cobalt and platinum) were successfully integrated into carbonized PVANFs. This is owing to the transition metal's ability to bind to PVA's hydroxyl groups and then the carbon content after carbonization [51]. The proposed preparation process is considered a good procedure for the synthesis of the carbon nanofibers decorated by metal nanoparticles after carbonization.
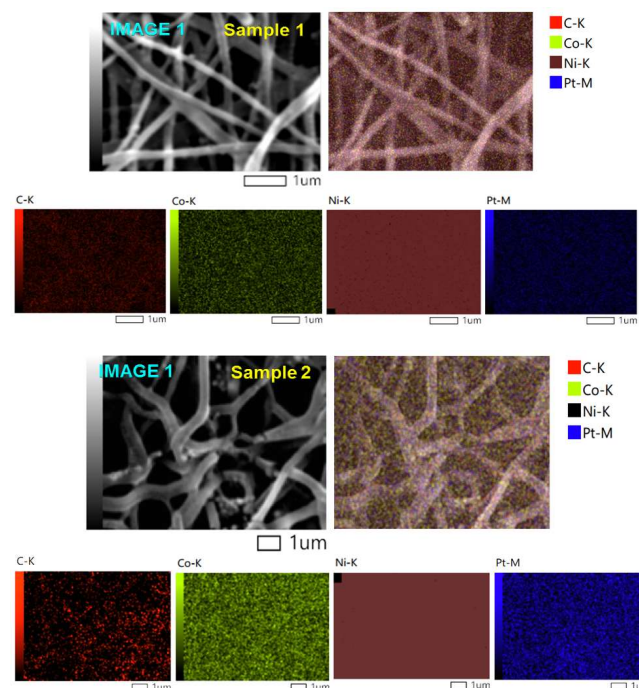
Figure 4. The SEM images and corresponding EDX mapping analysis of sample $Ni_4Co_2Pt/CNFs$ (S_1) and sample $Ni_5CoPt/CNFs$ (S_2).

The chemical content of the sample Ni₅CoPt/CNFs (sample S2) was identified through EDX analysis (Figure 5). The mass and the atomic percentages of its elements are listed in the inset of Figure 5. The mass percentages of C, Ni, Co and Pt are 78.93%, 14.59%, 3.11% and 3.37%, while the expected values are 80%, 14%, 3% and 3%, respectively. The small difference between the expected and produced ratios could be attributed to experimental circumstances.
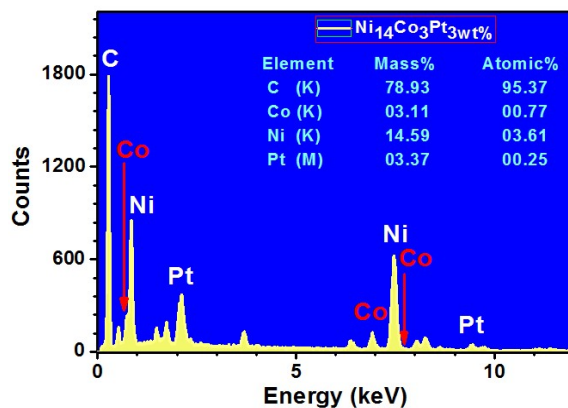

Figure 5. EDX spectrum for sample S2, Ni₅CoPt/CNFs.

3.3. Structure Analysis (XRD)

The XRD technique has been extensively used to determine the phases and crystallinity in materials. XRD patterns were recorded, as shown in Figure 6A–C, five diffraction peaks for Ni₄Co₂Pt/CNFs, Ni₅CoPt/CNFs, and Ni₆Pt/CNFs, are characteristic of a face-centered cubic (FCC) lattice. The broad peak at approximately 26° relates to the (002) plane of carbon (JCPDS; 41-1487) [52,53]. The CNFs were graphitic and this would increase the conductivity of the prepared electrodes [54]. The amorphous nature of PVA and the occurrence of sharp peaks connected to metallic NPs [55] could explain the low intensity of this peak. The slight change in the peak location of the prepared sample to higher angles compared to the data in (JCPDS file no. 04-0850) [56,57] for Ni indicates the formation of the ternary alloys [58]. XRD analysis confirmed the carbonization of the prepared nanofibers. Only one Pt peak appears in sample S₃ as shown in Figure 6C. For cobalt, its diffraction angles match that of nickel, so the peaks may be convoluted with nickel peaks due to its high proportion compared to cobalt. In contrast, the absence of amorphous or crystalline Pt and Co phases suggests that all metals are integrated into the FCC Ni phase; resulting in a real alloy at all particle sizes. The XRD analysis confirms that the nanoparticles exist only in the metallic phase in the composite no hydroxide or oxide phases are noticed in XRD patterns.
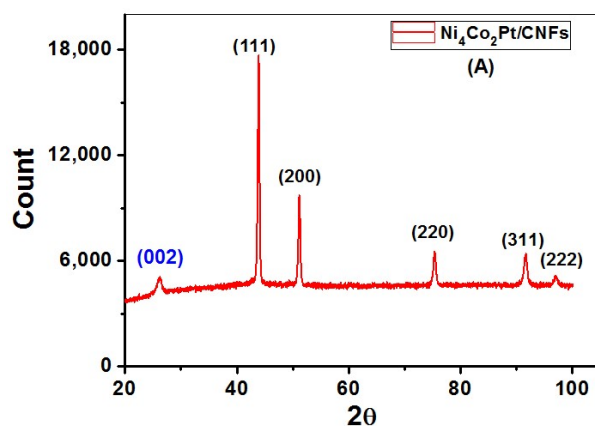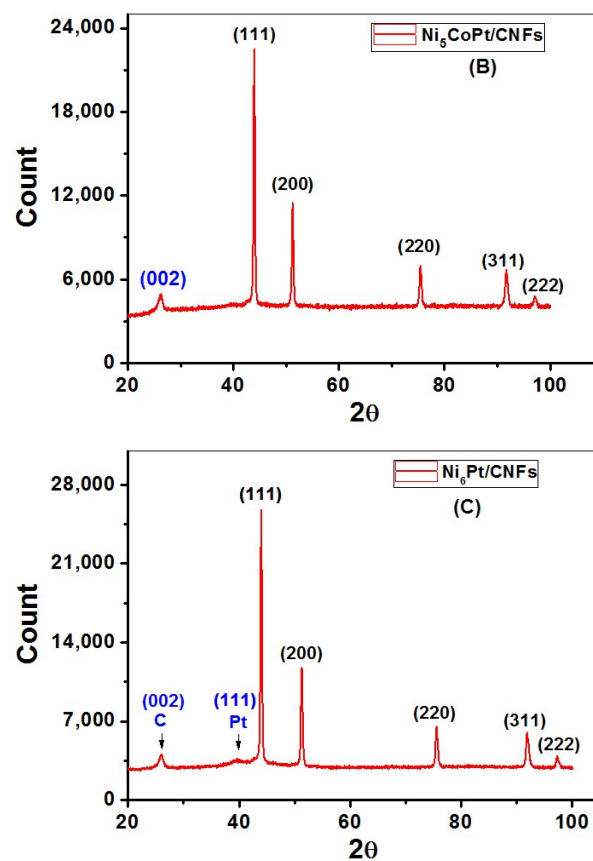

Figure 6. *Cont.*

Figure 6. X-ray diffraction patterns of (**A**) $Ni_4Co_2Pt/CNFs$, (**B**) $Ni_5CoPt/CNFs$, and (**C**) $Ni_6Pt/CNFs$.

The particle size was calculated and listed in Table 2 using the Debye-Scherer equation with data from the XRD analysis. The most intense diffraction peak (111) was taken for the determination of the particle size. The strain-free Scherer equation is in the form:

$$D = \frac{K\lambda}{\beta cos\theta} \tag{1}$$

where $K = 0.9$, $\lambda = 0.154$ nm, β, is the full width at high maximum (FWHM) and θ is the peak position. From Table 2 it can be noticed that the calculated particle size of the prepared alloys is relatively large. The increase in the particle size of the prepared samples may be due to that, the carbonization process was carried out at a high temperature may lead to the MNPs agglomerating with each other. From the table, it can also be noted that the values of the crystal lattice constant increase slightly with the increase in the proportion of cobalt due to the difference in the size of the cobalt atom from nickel.

Table 2. Particle sizes were calculated from the XRD results using the Scherer equation.

Sample	(hkl)	Peak Position	FWHM (β) (O)	D (nm) Scherer	SA (m^2/gm)	(a) Lattice Parameter (nm)
S1	(111)	43.876	0.3794	22.57	23.0	0.3570
S2	(111)	43.920	0.3483	24.59	21.1	0.3567
S3	(111)	43.979	0.3436	24.93	20.7	0.3562
Pd-Co-Mo/AC ref. [59] At 900 °C (70:20:10) nanoparticles				41.2	13.0	
Commercial Pt/AC As received				3.32	85.7	

The surface area (SA) is defined as the total surface area of a solid material per unit of mass. The surface area (SA) values can be determined according to the following equation [59,60]:

$$SA = \frac{6000}{D\rho} \qquad (2)$$

where D is the particle size in nm obtained from X-ray data and ρ is the density of the alloy. The XRD-determined surface area values for the samples S_1, S_2 and S_3 are listed in Table 2. SA values for the prepared alloys are smaller than those for the commercial Pt catalyst but larger than that of Pd-Co-Mo alloy on activated carbon heated at 900 °C [59] as shown in Table 2. For Ni systems, the carbonization temperature of 900 °C may be too high, inducing atom agglomeration and resulting in excessive grain size.

3.4. Electro-Oxidation Measurements

3.4.1. Effect of Sample Composition and Electrolyte

The EC measurements were quantified utilizing CHI 660E Electrochemical workstation attached with a 3-electrode EC cell of Ag/AgCl reference electrode, glassy carbon electrode coated by the fabricated nanofibers (working electrode), and a platinum wire (counter electrode). Figure 7 shows the effect of the sample composition on the EC catalytic activities for oxidating 2.0 M (A) ethanol, (B) methanol and (C) urea in 1 M KOH solution at RT (20 °C) and scan rate of100 mV/s. In 2.0 M ethanol, as the Ni% decreased from 17% to 11% and the Co% increased from 0 to 6%, Figure 7A. The incorporation of Co significantly improves the EC catalytic activity in terms of current density, increasing the maximum current density from 19.7 to 27.3 A/g. The current density of the oxidizing peak is 0.9 A/g @ 0.37 V, 8.2 A/g @ 0.52 V and 7.4 A/g @ 0.53 V for samples with Ni% of 11% (S1), 14% (S2) and 17% (S3). Also, the onset potentials are 0.30, 0.33, and 0.35 V, respectively.
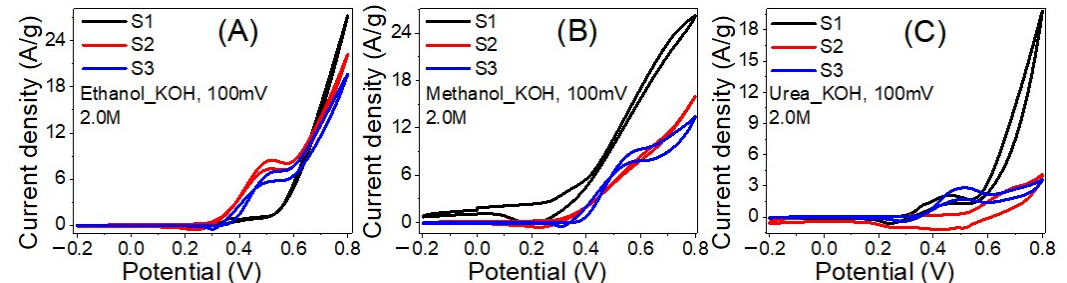
Figure 7. The influence of the sample composition on the EC catalytic activities for oxidating 2.0 M (**A**) ethanol, (**B**) Methanol and (**C**) Urea in 1 M KOH solutions at RT (20 °C).

In 2.0 M methanol, Figure 7B, the incorporation of Co considerably improves the EC catalytic activity by increasing the maximum current density from 13.4 to 26.2 A/g as the Co ratio increased from 0 to 6%. The current density of the oxidation peak is increased from1.5 A/g @ 0.32 V to 9.4 A/g @ 0.58 V as the Ni% increased from 11% to 17% with onset potentials of 0.26 and 0.37 V, respectively. This means 6.3 folds enhancement in the oxidation current by increasing Ni%. Furthermore, whereas the methanol EC oxidation peak is evident in samples S1 and S3, it is not apparent in sample S2.

In 2.0 M urea, Figure 7C, the maximum current density was raised from 3.6 to 19.8 A/g as the Co ratio increased from 0 to 6%. The current densities of the oxidation peaks are 1.2 A/g @ 0.36 V, 2.6 A/g @ 0.69 V and 2.8 A/g @ 0.52 V for Ni% of 11%, 14% and 17% with onset potentials of 0.31, 0.51 and 0.36 V, respectively. The observed results are intriguing because they show a possible rise in the EC catalytic activity of the suggested catalyst in terms of the amount of ethanol, methanol, and urea oxidized on its surface. This finding is more pronounced with methanol and ethanol than urea electrolysis. Based on the data, the insertion of Co with Ni could positively reduce the required activation energies of the oxidation reactions. Moreover, the effect of the electrolyte can be observed from Figure 7, whereas the current density for the sample with 6% Co doping has the order:

ethanol > methanol > urea. The observed onset potentials for methanol are lower than ethanol and urea.

3.4.2. Effect of Electrolyte Concentration

Ni is believed to be the best EC catalyst for the oxidation of ethanol and methanol [61]. Figure 8 shows CV voltammograms of the prepared nanofibers samples at different ethanol, methanol, and urea concentrations. As shown in Figure 8A, as the ethanol concentrations increase the current densities of the oxidation peaks are increased and accompanied by a shift to a lower potential position. The maximum current density was increased from 26.6 to 28.2 A/g as the ethanol concentration increased from 0.5 M to 1.5 M, and then slightly decreased to 27.3 A/g as the concentration increased to 2.0 M. The current densities of the oxidation peaks are changed from 0.85 A/g @ 387 mV to 0.90 A/g @ 368 mV with onset potentials reduced from 315 to 298 mV as the ethanol concentration changed from 0.5 M to 2.0 M. This proves the enhancement of the EC catalytic activities of sample S1 to ethanol electrooxidation as its concentration increased. The ethanol electrooxidation process is based on the adsorption of the intermediate components and reactants, which is followed by dissociation stages. The O–H bond was first broken in the ethanol dehydrogenation, resulting in the formation of ethoxy species (CH_3CH_2O). These species were then transformed to acetaldehyde (CH_3CHO). Many processes oxidize the produced acetaldehyde, resulting in acetate ions (CH_3COO^-), acetyl (CH_3CO), methane, acetone (CH_3COCH_3), crotonaldehyde ($CH_3CHCHCHO$), other hydrocarbons, carbonate ion (CO_3^{2-}), CO_2, and CO [62,63].
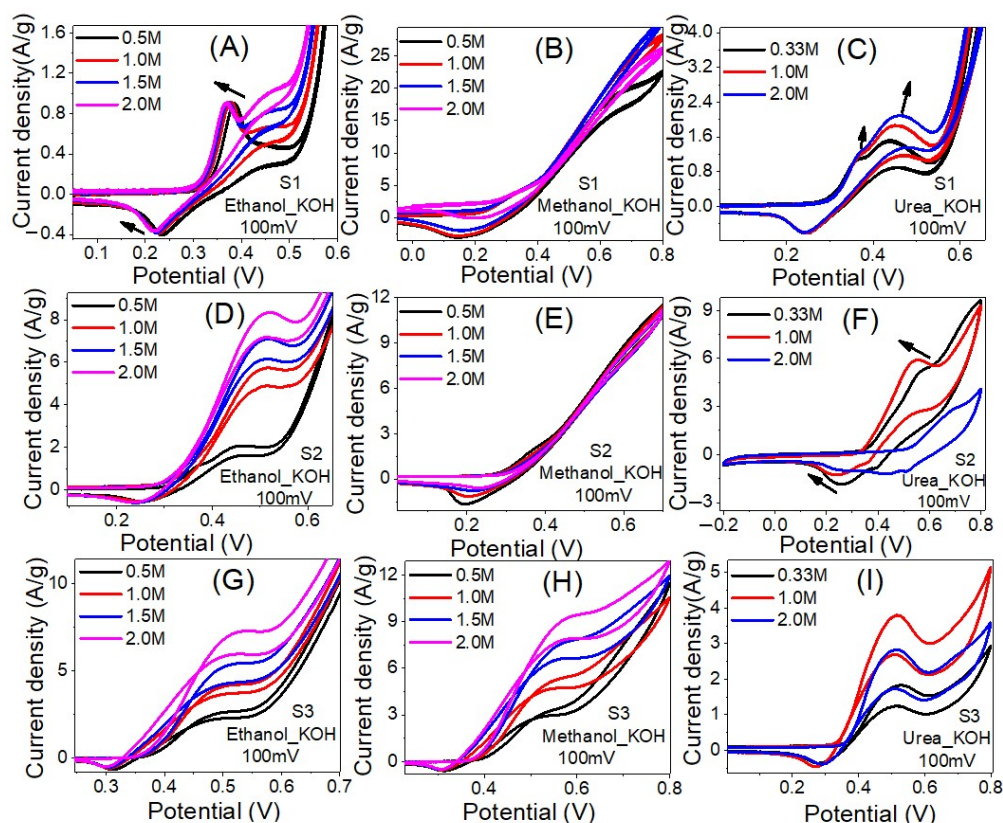
Figure 8. The influence of ethanol, Methanol, and Urea concentration on the electrocatalytic activity of samples S1 (**A–C**), S2 (**D–F**) and S3 (**G–I**) in 1.0 M KOH solution at RT.

Similar results are observed for the electrooxidation of methanol and ethanol using sample S1 as shown in Figure 8B,C. For methanol, the values of the maximum current density were 22.7, 28.3, 30.6 and 26.2 A/g at methanol concentrations of 0.5 M, 1.0 M, 1.5 M and 2.0 M, individually. The current densities of the oxidation peaks are changed from

2.2 A/g @318 mV to 2.8 A/g @318 mV with onset potentials increased from 219 to 235 mV as the methanol concentration changed from 0.5 M to 1.5 M.

For urea, the recorded maximum current densities were 21.2, 20.7, 19.8 A/gat urea concentrations of 0.33 M, 1.0 M and 2.0 M i.e., as the concentration increased, the maximum current density decreased. Additionally, two oxidation peaks were observed as indicated by the arrows in Figure 8C. The current density of the first oxidation peak is changed from 1.0 A/g @ 358 mV to 1.2 A/g @ 364 mV with onset potentials increased from 303 to 308 mV as the urea concentration changed from 0.33 M to 2.0 M. The current density of the second oxidation peak is changed from 1.4 A/g @ 430 mV to 2.0 A/g @ 451 mV with onset potentials reduced from 279 to 294 mV as the urea concentration changed from 0.33 M to 2.0 M.

For Sample S2, Figure 8D–F, the highest current density was observed using 2 M ethanol. The value of the highest current density is 21.9 A/g @ 2 M ethanol, 15.3 A/g @ 2 M methanol and 9.7 A/g @ 0.33 M urea. For ethanol, the current density of the oxidation peak is increased from 1.1 A/g @ 449 mV to 8.2 A/g @ 515 mV with onset potential increased from 310 to 329 mV as the concentration increased from 0.5 M to 2.0 M. For methanol, the current density of the oxidation peak is decreased from 1.5 A/g @ 356 mV to 1.1 A/g @ 359 mV as the concentration increased from 0.5 M to 2.0 M with onsets increased from 280 to 298 mV. For urea, the oxidation peak current density is increased from 1.8 A/g @ 560 mV to 6.0 A/g @ 545 mV with increasing the concentration from 0.33 M to 1.0 M and then decreased to 2.5 A/g @ 688 mV as the concentration raised to 2.0 M. Similarly, the inset potential reduced from 357 to 353 mV and then increased to 522 mV. Therefore, this sample is more efficient for electrooxidation of 2.0 M ethanol and 1.0 M urea than 2.0 M methanol. Whereas the energy required for the electrooxidation of urea is less than ethanol.

For Sample S3, Figure 8G–I, the highest current density was observed using 2 M ethanol. The value of the highest current density is 19.1 A/g @ 2 M ethanol, 12.9 A/g @ 2 M methanol and 5.2 A/g @ 1.0 M urea. For ethanol, the current density of the oxidation peak is increased from 2.7 A/g @ 508 mV to 7.4 A/g @ 530 mV with onset potential decreased from 377 to 354 mV as the concentration increased from 0.5 M to 2.0 M. For methanol, the current density of the oxidation peak is increased from 3.0 A/g @ 508 mV to 9.4 A/g @ 584 mV as the concentration increased from 0.5 M to 2.0 M with onsets decreased from 403 to 372 mV.

For urea, the oxidation peak current density is increased from 1.7 A/g @ 528 mV to 3.7 A/g @ 514 mV with increasing the concentration from 0.33 M to 1.0 M and then decreased to 2.7 A/g @ 511 mV as the concentration raised to 2.0 M. The inset potential declined from 369mV @ 0.33 Mto 339 mV @ 1.0 M and then increased to 366 mV @ 2.0 M. Therefore, this sample is more efficient for electrooxidation of 2.0 M methanol and 2.0 M ethanol than 1.0 M urea. The energy required for the electrooxidation follows the order urea < ethanol < methanol. For the urea electrooxidation behaviors on the S1, S2 and S3 catalysts, Figure 8C,F,I, there are a pair of distinct redox current peaks, which correspond to the reversible variation between Ni^{2+} and Ni^{3+}, based on Equation (3) [64].

$$Ni(OH)_2 + OH^- \longleftrightarrow NiOOH + H_2O + e^- \qquad (3)$$
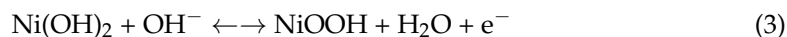
In the forward scan, the observed anodic peak is ascribed to the oxidation of $Ni(OH)_2$ to NiOOH [65]. Whereas, during the reverse scan, the cathodic peak refers to the reduction of NiOOH to $Ni(OH)_2$ [66]. The second anodic peak observed for S1 is appeared due to the transformation of $Co(OH)_2$ to CoOOH. In summary, the optimized concentrations for all samples and electrolytes are reported in Table 3.

Table 3. Optimized concentrations and Tafel slope values for S1, S2 and S3 in ethanol, methanol, and urea electro-oxidation reactions.

| Parameter	Optimized Concentration			Tafel Slop (mV/Dec)		
Sample	S1	S2	S3	S1	S2	S3
Ethanol	1.5	2	2	29.6 ± 0.1	25.6 ± 0.1	19.1 ± 0.2
Methanol	1.5	2	2	30.6 ± 0.1	28.5 ± 0.1	22.6 ± 0.2
Urea	0.33	1	1	38.5 ± 0.2	31.9 ± 0.3	23.6 ± 0.2

3.4.3. Effect of the Scan Rate

Figure 9 shows the influence of the scan rate on the electrocatalytic activity of the prepared samples for electrooxidation of ethanol, methanol and urea in 1.0 M KOH solution at RT. As the scan rate increased the current density of the oxidation peak increased and the peak position shifted to a higher potential. The roughly linear plots between ethanol, methanol and urea oxidation peaks current density and the square root of the scan rate, as shown in Figure 10A–C, suggest a diffusion-controlled mechanism [67,68]. The diffusion-controlled characteristics are further clarified using the plot of log (anodic current density) vs. log (scan rate), as shown in Figure S2 (supplementary data) i.e., these data demonstrate that the oxidation process is diffusion-controlled [69]. The increase of the oxidation current density with increasing the scan rate points to improve the kinetic oxidation of methanol. Whereas the linear dependence of the anodic peak potential vs. the logarithm of the scan rate, Figure 10D–E, indicates kinetics limitations for the reaction [70,71]. The peak height is proportional to the square root of the potential scan rate when the positions of the anodic peaks do not change with the potential scan rate, thermodynamically reversible electrochemical reactions, according to the following equation (T = 25 °C): IP = (2.69 × 10^5) $n^{3/2} AD^{1/2} v^{1/2} C$. Whereas IP is the peak current, n is the number of electrons per reactant molecule, A is the electrode area, v is the potential scan rate, D is the diffusion coefficient, and C is the bulk concentration of the reactant [72]. Note that the electrochemical reactions are not completely reversible according to Figure 9 because the anodic peak potential becomes more positive, and the cathodic peak potential becomes more negative as the scan rate increases. Therefore, the separation of the anodic and cathodic peaks becomes larger than in the reversible case.

The anodic current increases progressively with increasing scan rates (range from 10 to 150 mV s^{-1}), as seen in Figure 9C,F,I. In addition, at higher scan rates, the shift of anodic peak potentials to a more positive orientation (Figure 9F) displays a change in the reaction kinetics between urea and Ni^{3+} [67]. The shift in peak potentials toward higher positive values can be attributed to the selective adsorption of urea on Ni^{3+} sites. Furthermore, the linear relationship between the anodic peak current density and the square root of scan rate ($v^{1/2}$) implies that the electrooxidation reaction on the catalytic samples S1–S3 is controlled by diffusion (Figure 10A–C) [68,70,73]. The anodic peak potential increases approximately linearly with the logarithm of the scan rate (log v) in Figure 10D–F, showing that ethanol, methanol, and urea electrooxidation have kinetic constraints [70]. According to these, the electrooxidation of ethanol, methanol, and urea on our catalysts is controlled by a combination of diffusion and kinetic limitations [74].

3.4.4. Linear Sweep Voltammetry

Figure 11A–C shows the LSV curves for the prepared samples (S1, S2, S3). The LSV curves were measured by a three-electrode cell in 1 M KOH at optimal ethanol, methanol, and urea concentrations. The scanning rate of LSV is performed at 10 mV/s in the potential range from −0.2 to 0.8 V. As shown in the supplementary data (Table S1), this voltage window has been employed in many earlier works for ethanol, methanol, and urea electro-oxidation. For sample S1, the current density increased from 23.2 to 26.8 and then to 35.7 A/g @ 799 mV for methanol, urea, and ethanol, respectively. For sample S2, the current density increased from 18.7 to 24.5 and then to 27.4 A/g @ 799 mV for urea, methanol, and ethanol, respectively. For sample S3, the current density increased from 11.3 to 37.40

and then to 37.42 A/g @ 799 mV for urea, methanol, and ethanol, respectively. When compared to urea and methanol solutions, the ethanol solution has the highest current density at a potential of 799 mV for all samples. Also, sample S2 has the lowest current density compared with other samples, which can be attributed to the comparatively large particle size and small surface area, and lower content of nickel compared to S1.
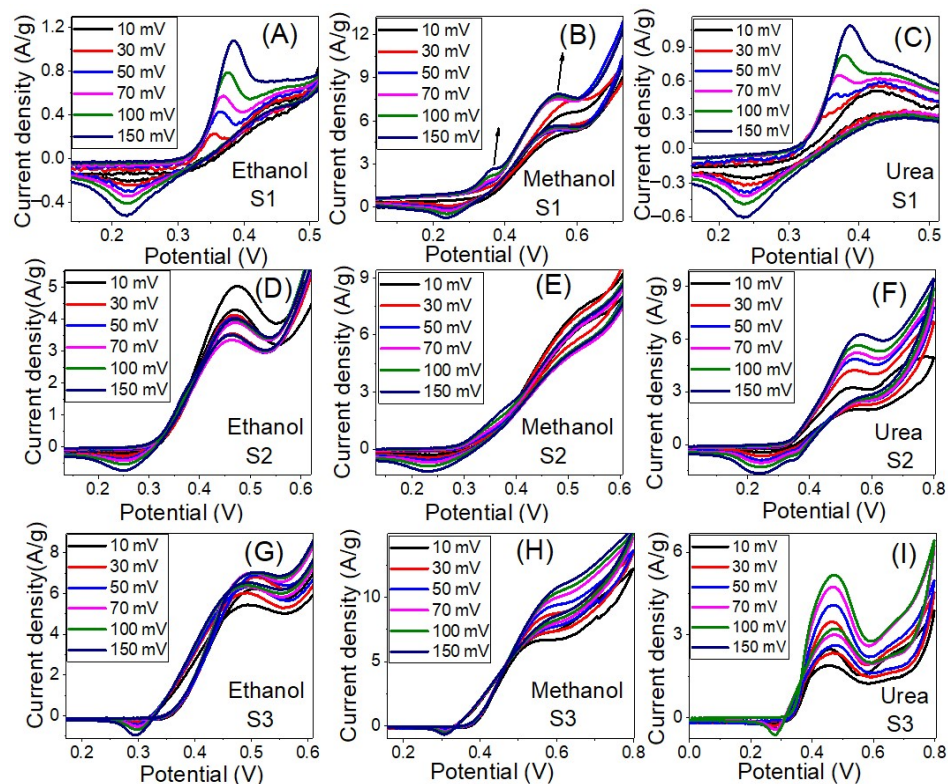

Figure 9. The influence of the scan rate on the electrocatalytic activity of samples S1 (**A–C**), S2 (**D–F**) and S3 (**G–I**) for electrooxidation of ethanol, Methanol, and Urea in 1.0 M KOH solution at RT.

To investigate the kinetics of electrochemical reactions, the Tafel curves were used (Figure S3, supplementary data). The corresponding Tafel slopes were presented in Table 3. For methanol, the slopes are lower. Also, the Tafel slope is reduced from 29.6 ± 0.1 to 19.1 ± 0.2 mV/dec for ethanol, from 30.6 ± 0.1 to 22.6 ± 0.2 mV/dec for methanol, and from 38.5 ± 0.2 to 23.6 ± 0.2 mV/dec for urea by increasing the Ni% from 11 to 17%, as shown in Table 3. It is clear that S1 has a slightly higher Tafel slope than S3.

3.4.5. Stability Study

The stability of the samples S1 and S3 in ethanol, methanol, and urea at 0.8 V between the working electrode and the Pt counter electrode is examined for an extended period. The fluctuations of current density versus time, as measured by chronoamperometry, are shown in Figure 12A,B. Sample S1 showed higher stability toward the methanol electrooxidation than ethanol and urea electrooxidation. The current density is decreased from 0.61 A/g to 0.26 A/g for methanol as the time reaction increased from 5 s to 1000 s before reaching a stable production rate, which is attributed to a limited corrosion process that occurs between the electrode and the redox electrolyte [75]. Sample S3 showed higher stability toward the urea electrooxidation than ethanol and ethanol electrooxidation. The current density is decreased from 0.24 A/g to 0.17 A/g for urea as the time increased from 7 s to 1000 s before reaching a stable production rate. This demonstrates that the S3 electrode has great chemical stability and a long lifetime as a working electrooxidation electrode, despite the initial drop in current density i.e., these findings suggest that using Co as a co-catalyst to boost the electrocatalytic activity of Ni/Ag catalysts has significant benefits.
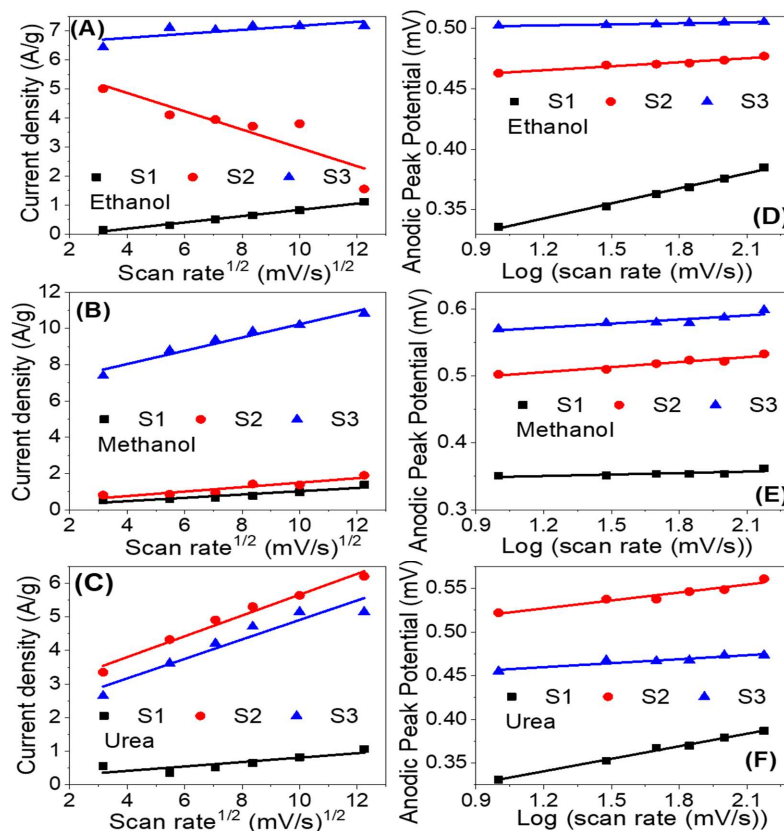
Figure 10. Current density versus the square root of the scan rate(**A**–**C**) and anodic peak potential versus the logarithm of the scan rate (**D**–**F**) for the electrooxidation of ethanol, methanol, and urea utilizing samples S1, S2 and S3.
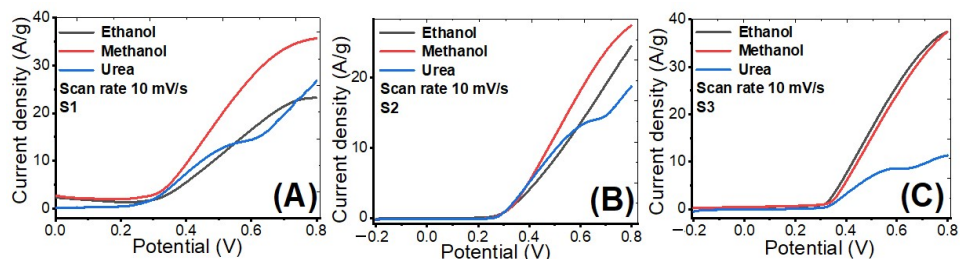

Figure 11. Linear sweep voltammetry plots at scan rate 10 mV/s of prepared (**A**) S1, (**B**) S2 and (**C**) S3 in ethanol, methanol, and urea at the optimized concentrations.
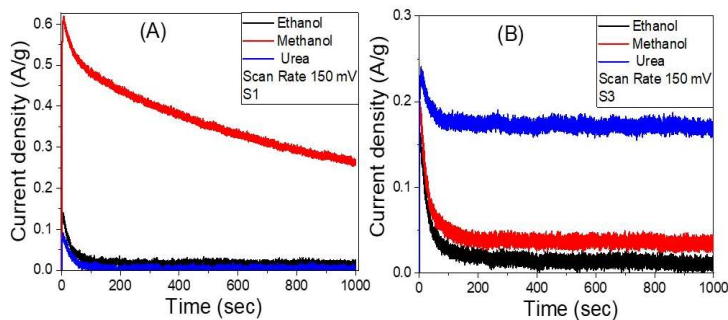
Figure 12. The variation of the current density versus time, chronoamperometry measurements, for samples (**A**) S1 and (**B**) S3 in ethanol, methanol, and urea.

### 3.4.6. Electrochemical Impedance Spectroscopy (EIS)

The electrooxidation catalytic efficiency of the working electrodes is largely determined by charge carrier dynamics. EIS experiments were carried out at RT utilizing an electrochemical workstation to explore the charge carrier dynamics of the samples (CH Instruments CHI660E). EIS is a valuable approach for evaluating the electrocatalyst's interfacial characteristics [76]. The sum of real, Z′, and imaginary, Z″, components contributed by the cell's resistance and capacitance is the impedance [77]. EIS measurements were done at 0 V (vs Ag/AgCl) under illumination with a frequency range of 0.01–100,000 Hz with the S1–S3 electrodes immersed in ethanol, methanol, and urea electrolytes. The Nyquist plots for all electro-electrodes are displayed in Figure 13. As shown in Figure 13A–C for sample S1, all working electrodes showed a semicircle at high frequencies due to charge transfer processes at electrode/electrolyte boundaries (charge transfer resistance), and two straight line segments with slopes of 45° and 55° at low frequencies due to diffusion-controlled processes (Warburg impedance) and additional limited capacitive behavior (double-layer capacitance) i.e., Mixed diffusion, and kinetic controlled routes are depicted in the EIS data. In comparison to the other electrodes, electrode S1 has the lowest charge transfer resistance and electrolyte resistance, improving the electrooxidation catalytic process.
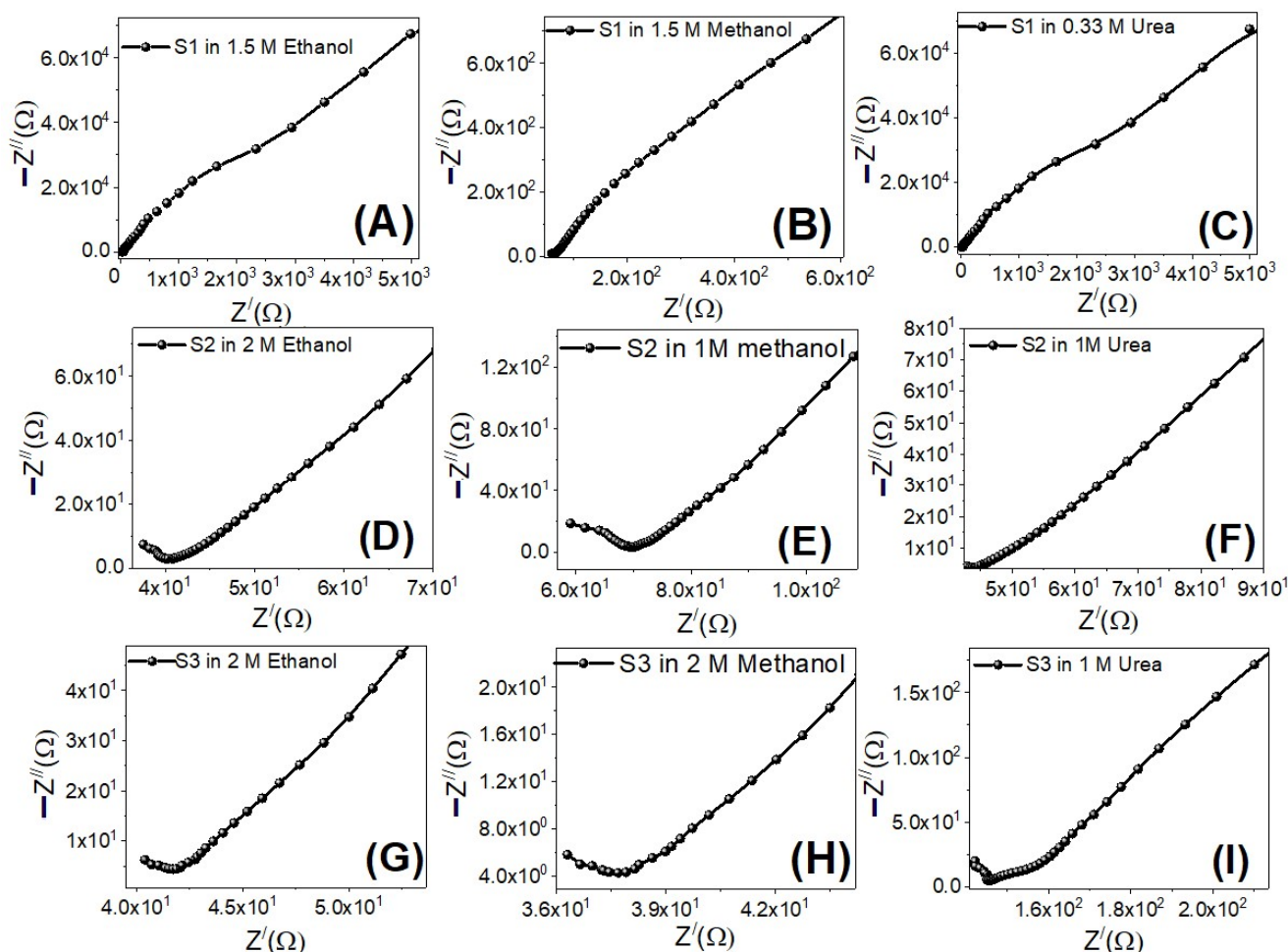
Figure 13. Nyquist plots for electrodes S1 (**A–C**), S2 (**D–F**) and S3 (**G–I**) in ethanol, methanol, and urea at the optimized concentrations and 0 V (vs. Ag/AgCl).

Figure 14 shows Bode charts for all electrodes using ethanol, methanol, and urea at 0 V (vs. Ag/AgCl) at RT. Figure 14 depicts the variation of the logarithm of the total impedance (Z) with the frequency logarithm, as well as the variation of the phase with the frequency logarithm. Plotting the Log (Z) with Log (*f*) reveals a resistive regime at low frequencies

due to the charge transfer resistance, as well as a very minimal capacitive contribution at high frequencies due to the electrode's double-layer capacitance [78]. With rising Co levels, there is a significant reduction in charge recombination at the electrolyte/electrode interfaces. This also includes a kinetically simple electroxidation process, increased ionic conductivity, and electrolytes diffusion across sample S1. As a result, when compared to the other electrodes, this electrode demonstrated superior electrooxidation catalytic performance.
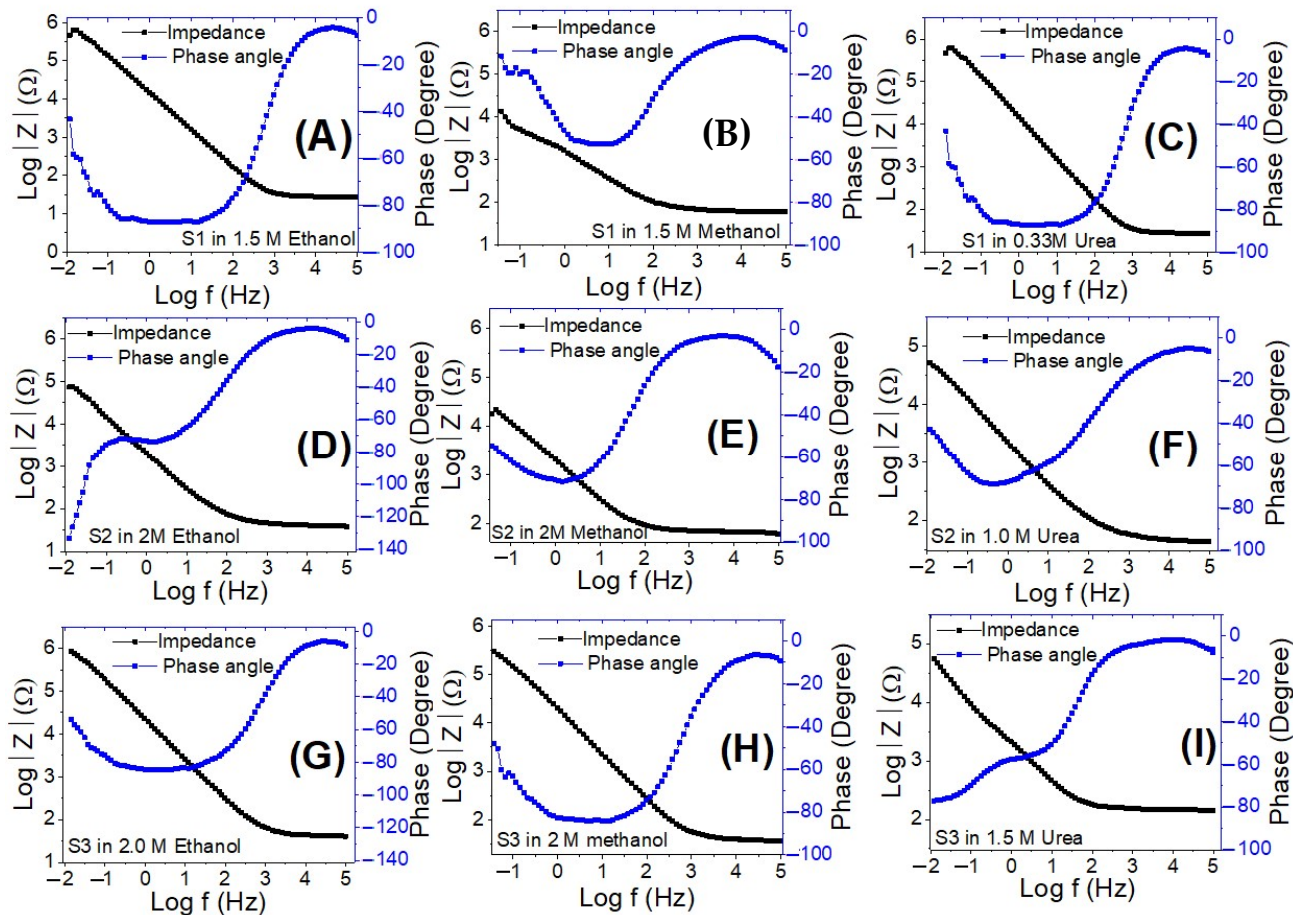
Figure 14. Bode plots for electrodes S1 (**A**–**C**), S2 (**D**–**F**), and S3 (**G**–**I**) in ethanol, methanol, and urea at the optimized concentrations and 0 V (vs. Ag/AgCl).

4. Conclusions

In this work, NiCoPt/CNFs nanoparticles were successfully loaded on carbon nanofibers utilizing electrospinning followed by carbonization at 900 °C for 7 h in an argon atmosphere. The chemical composition: structures, nanomorphologies, and electrochemical properties were investigated utilizing different analysis techniques. The carbonization process of the obtained electrospun nanofibers reduces the fiber diameter from 200–580 nm to 150–200 nm for samples with varying Co percent (0–6%). The EDX mapping revealed a homogeneous and uniform distribution of Ni, Pt and Co on the carbonized PVANFs' surface. The Ni-Co-Pt/CNFs have a face-centered cubic (FCC) lattice with crystallite sizes decreasing from 24.93 to 22.57 nm as the cobalt ratio increased. The electrocatalytic properties of the samples were investigated for electrooxidation of ethanol, methanol, and urea. The effects of electrolyte concentration, scan rate, electrode stability, and EIS spectroscopy were studied. Inserting Co as a co-catalyst with nickel could successfully lower the electrooxidation reaction's required activation energy and increase the electrode's stability. Moreover, in 2 M electrolyte concentration, the current density for the 6% Co sample is in the following order: $J_{ethanol} > J_{methanol} > J_{urea}$. The Ni$_5$CoPt/CNFs electrode in 1.5 M methanol had the

lowest onset potential, while the maximum current densities were 28.2, 30.6 and 21.2 A/g for 1.5 M ethanol, 1.5 M methanol and 0.33 M urea, respectively. This study demonstrated a novel approach to creating a highly active Ni-Co-Pt-based electrocatalyst oxidation of ethanol, methanol, and urea.

Supplementary Materials: The following supporting information can be downloaded at: https://www.mdpi.com/article/10.3390/nano12030492/s1. Figure S1: Plots of Log (Current density) versus Log (scan rate) for the electrooxidation of (A) ethanol, (B) methanol and (C) urea utilizing samples S1, S2 and S3; Figure S2: Plots of overpotential versus log (current density) for calculating the Tafel slopes of the prepared (A) S1, (B) S2 and (C) S3 in ethanol, methanol, and urea at the optimized concentrations; Table S1: Voltage windows, electrocatalysts, and used solutions in previously reported works relative to the present study for ethanol, methanol, and urea electro-oxidation. References [79–83] are cited in the supplementary materials.

Author Contributions: Conceptualization, A.M.A. and M.S.; methodology, A.M.A. and M.S.; validation, A.M.A. and M.S.; formal analysis, E.E.A.-H.; M.O.A.-H., A.G, A.M.A. and M.S.; investigation, E.E.A.-H., M.O.A.-H., A.G, A.M.A. and M.S.; resources, E.E.A.-H., M.O.A.-H., A.G, A.M.A., and M.S.; data curation, E.E.A.-H., M.O.A.-H., A.G, A.M.A. and M.S.; writing—original draft preparation, E.E.A.-H., M.O.A.-H., A.G, A.M.A. and M.S.; writing—review and editing, E.E.A.-H., M.O.A.-H., A.G., A.M.A. and M.S.; visualization, E.E.A.-H., M.O.A.-H., A.G., A.M.A. and M.S.; project administration, E.E.A.-H., M.O.A.-H., A.G., A.M.A., H.Y. and M.S.; funding acquisition, E.E.A.-H., M.O.A.-H., A.G., A.M.A., H.Y. and M.S. All authors have read and agreed to the published version of the manuscript.

Institutional Review Board Statement: Not applicable.

Informed Consent Statement: Not applicable.

Data Availability Statement: Not applicable.

Conflicts of Interest: The authors declare no conflict of interest.

References

1. Meyer, Q.; Zeng, Y.; Zhao, C. In situ and operando characterization of proton exchange membrane fuel cells. *Adv. Mater.* **2019**, *31*, 1901900. [CrossRef] [PubMed]
2. Wang, L.; Wan, X.; Liu, S.; Xu, L.; Shui, J. Fe-NC catalysts for PEMFC: Progress towards the commercial application under DOE reference. *J. Energy Chem.* **2019**, *39*, 77–87. [CrossRef]
3. Watanabe, M.; Tsurumi, K.; Mizukami, T.; Nakamura, T.; Stonehart, P. Activity and stability of ordered and disordered Co-Pt alloys for phosphoric acid fuel cells. *J. Electrochem. Soc.* **1994**, *141*, 2659. [CrossRef]
4. Naitabdi, A.; Boucly, A.; Rochet, F.; Fagiewicz, R.; Olivieri, G.; Bournel, F.; Benbalagh, R.; Sirotti, F.; Gallet, J.-J. CO oxidation activity of Pt, Zn and ZnPt nanocatalysts: A comparative study by in situ near-ambient pressure X-ray photoelectron spectroscopy. *Nanoscale* **2018**, *10*, 6566–6580. [CrossRef]
5. Long, N.V.; Asaka, T.; Matsubara, T.; Nogami, M. Shape-controlled synthesis of Pt–Pd core-shell nanoparticles exhibiting polyhedral morphologies by modified polyol method. *Acta Mater.* **2011**, *59*, 2901–2907. [CrossRef]
6. Lee, Y.-W.; Kim, B.-Y.; Lee, K.-H.; Song, W.-J.; Cao, G.; Park, K.-W. Synthesis of monodispersed Pt-Ni alloy nanodendrites and their electrochemical properties. *Int. J. Electrochem. Sci.* **2013**, *8*, 2305–2312.
7. Cai, Z.; Kuang, Y.; Qi, X.; Wang, P.; Zhang, Y.; Zhang, Z.; Sun, X. Ultrathin branched PtFe and PtRuFe nanodendrites with enhanced electrocatalytic activity. *J. Mater. Chem. A* **2015**, *3*, 1182–1187. [CrossRef]
8. Mizrahi, M.D.; Krylova, G.; Giovanetti, L.J.; Ramallo-López, J.M.; Liu, Y.; Shevchenko, E.V.; Requejo, F.G. Unexpected compositional and structural modification of CoPt 3 nanoparticles by extensive surface purification. *Nanoscale* **2018**, *10*, 6382–6392. [CrossRef]
9. Wu, F.; Lai, J.; Zhang, L.; Niu, W.; Lou, B.; Luque, R.; Xu, G. Hierarchical concave layered triangular PtCu alloy nanostructures: Rational integration of dendritic nanostructures for efficient formic acid electrooxidation. *Nanoscale* **2018**, *10*, 9369–9375. [CrossRef]
10. Chen, C.; Kang, Y.; Huo, Z.; Zhu, Z.; Huang, W.; Xin, H.L.; Snyder, J.D.; Li, D.; Herron, J.A.; Mavrikakis, M. Highly crystalline multimetallic nanoframes with three-dimensional electrocatalytic surfaces. *Science* **2014**, *343*, 1339–1343. [CrossRef]
11. Singh, K.; Tetteh, E.B.; Lee, H.-Y.; Kang, T.-H.; Yu, J.-S. Tailor-made Pt catalysts with improved oxygen reduction reaction stability/durability. *ACS Catal.* **2019**, *9*, 8622–8645. [CrossRef]

12. Safo, I.A.; Dosche, C.; Özaslan, M. Effects of capping agents on the oxygen reduction reaction activity and shape stability of Pt nanocubes. *ChemPhysChem* **2019**, *20*, 3010. [CrossRef]

13. Fratoddi, I.; Matassa, R.; Fontana, L.; Venditti, I.; Familiari, G.; Battocchio, C.; Magnano, E.; Nappini, S.; Leahu, G.; Belardini, A. Electronic properties of a functionalized noble metal nanoparticles covalent network. *J. Phys. Chem. C* **2017**, *121*, 18110–18119. [CrossRef]

14. Siegel, J.; Staszek, M.; Polívková, M.; Řezníčková, A.; Rimpelová, S.; Švorčík, V. Green synthesized noble metals for biological applications. *Mater. Today Proc.* **2016**, *3*, 608–616. [CrossRef]

15. Manjunathaa, J.G.; Deraman, M.; Basri, N.H.; Talib, I.A. Selective Detection of Dopamine in the Presence of Uric Acid Using Polymerized Phthalo Blue Film Modified Carbon Paste Electrode. *Adv. Mater. Res.* **2014**, *895*, 447–451.

16. Kwizera, E.A.; Chaffin, E.; Shen, X.; Chen, J.; Zou, Q.; Wu, Z.; Gai, Z.; Bhana, S.; O'Connor, R.; Wang, L. Size-and shape-controlled synthesis and properties of magnetic–plasmonic core–shell nanoparticles. *J. Phys. Chem. C* **2016**, *120*, 10530–10546. [CrossRef]

17. Ji, X.; Shao, R.; Elliott, A.M.; Stafford, R.J.; Esparza-Coss, E.; Bankson, J.A.; Liang, G.; Luo, Z.-P.; Park, K.; Markert, J.T. Bifunctional gold nanoshells with a superparamagnetic iron oxide—Silica core suitable for both MR imaging and photothermal therapy. *J. Phys. Chem. C* **2007**, *111*, 6245–6251. [CrossRef]

18. Pushpanjali, P.A.; Manjunatha, J.G.; Amrutha, B.M.; Hareesha, N. Development of carbon nanotube-based polymer-modified electrochemical sensor for the voltammetric study of Curcumin. *Mater. Res. Innov.* **2021**, *25*, 412–420. [CrossRef]

19. Raril, C.; Manjunatha, J.G. Sensitive Electrochemical Analysis of Resorcinol using Polymer Modified Carbon Paste Electrode: A Cyclic Voltammetric Study. *Anal. Bioanal. Electrochem.* **2018**, *10*, 488–498.

20. Cao, Z.; Li, H.; Zhan, C.; Zhang, J.; Wang, W.; Xu, B.; Lu, F.; Jiang, Y.; Xie, Z.; Zheng, L. Monocrystalline platinum–nickel branched nanocages with enhanced catalytic performance towards the hydrogen evolution reaction. *Nanoscale* **2018**, *10*, 5072–5077. [CrossRef]

21. Xia, B.Y.; Wang, J.N.; Wang, X.X. Synthesis and application of Pt nanocrystals with controlled crystallographic planes. *J. Phys. Chem. C* **2009**, *113*, 18115–18120. [CrossRef]

22. Rabis, A.; Rodriguez, P.; Schmidt, T.J. Electrocatalysis for polymer electrolyte fuel cells: Recent achievements and future challenges. *Acs. Catal.* **2012**, *2*, 864–890. [CrossRef]

23. Debe, M.K. Electrocatalyst approaches and challenges for automotive fuel cells. *Nature* **2012**, *486*, 43–51. [CrossRef] [PubMed]

24. Wagner, F.T.; Lakshmanan, B.; Mathias, M.F. Electrochemistry and the future of the automobile. *J. Phys. Chem. Lett.* **2010**, *1*, 2204–2219. [CrossRef]

25. Stephens, I.E.; Bondarenko, A.S.; Perez-Alonso, F.J.; Calle-Vallejo, F.; Bech, L.; Johansson, T.P.; Jepsen, A.K.; Frydendal, R.; Knudsen, B.P.; Rossmeisl, J. Tuning the activity of Pt (111) for oxygen electroreduction by subsurface alloying. *J. Am. Chem. Soc.* **2011**, *133*, 5485–5491. [CrossRef]

26. Steele, B.C.; Heinzel, A. Materials for fuel-cell technologies. *Nature* **2001**, *414*, 345–352. [CrossRef]

27. Li, X.; Colón-Mercado, H.R.; Wu, G.; Lee, J.-W.; Popov, B.N. Development of method for synthesis of Pt–Co cathode catalysts for PEM fuel cells. *Electrochem. Solid State Lett.* **2007**, *10*, B201. [CrossRef]

28. Tseng, C.-J.; Lo, S.-T.; Lo, S.-C.; Chu, P.P. Characterization of Pt-Cu binary catalysts for oxygen reduction for fuel cell applications. *Mater. Chem. Phys.* **2006**, *100*, 385–390. [CrossRef]

29. Antolini, E.; Salgado, J.R.; Gonzalez, E.R. The stability of Pt–M (M= first row transition metal) alloy catalysts and its effect on the activity in low temperature fuel cells: A literature review and tests on a Pt–Co catalyst. *J. Power Sources* **2006**, *160*, 957–968. [CrossRef]

30. Xiong, L.; Kannan, A.; Manthiram, A. Pt–M (M= Fe, Co, Ni and Cu) electrocatalysts synthesized by an aqueous route for proton exchange membrane fuel cells. *Electrochem. Commun.* **2002**, *4*, 898–903. [CrossRef]

31. Lima, F.H.; Giz, M.J.; Ticianelli, E.A. Electrochemical performance of dispersed Pt-M (M= V, Cr and Co) nanoparticles for the oxygen reduction electrocatalysis. *J. Mex. Chem. Soc.* **2005**, *49*, 90–98. [CrossRef]

32. Travitsky, N.; Ripenbein, T.; Golodnitsky, D.; Rosenberg, Y.; Burshtein, L.; Peled, E. Pt-, PtNi-and PtCo-supported catalysts for oxygen reduction in PEM fuel cells. *J. Power Sources* **2006**, *161*, 782–789. [CrossRef]

33. Wu, J.; Yuan, X.Z.; Martin, J.J.; Wang, H.; Zhang, J.; Shen, J.; Wu, S.; Merida, W. A review of PEM fuel cell durability: Degradation mechanisms and mitigation strategies. *J. Power Sources* **2008**, *184*, 104–119. [CrossRef]

34. Min, M.-k.; Cho, J.; Cho, K.; Kim, H. Particle size and alloying effects of Pt-based alloy catalysts for fuel cell applications. *Electrochim. Acta* **2000**, *45*, 4211–4217. [CrossRef]

35. Paulus, U.; Wokaun, A.; Scherer, G.; Schmidt, T.; Stamenkovic, V.; Radmilovic, V.; Markovic, N.; Ross, P. Oxygen reduction on carbon-supported Pt− Ni and Pt− Co alloy catalysts. *J. Phys. Chem. B* **2002**, *106*, 4181–4191. [CrossRef]

36. Stamenkovic, V.R.; Mun, B.S.; Arenz, M.; Mayrhofer, K.J.; Lucas, C.A.; Wang, G.; Ross, P.N.; Markovic, N.M. Trends in electrocatalysis on extended and nanoscale Pt-bimetallic alloy surfaces. *Nat. Mater.* **2007**, *6*, 241–247. [CrossRef]

37. Stamenkovic, V.; Mun, B.S.; Mayrhofer, K.J.; Ross, P.N.; Markovic, N.M.; Rossmeisl, J.; Greeley, J.; Nørskov, J.K. Changing the activity of electrocatalysts for oxygen reduction by tuning the surface electronic structure. *Angew. Chem.* **2006**, *118*, 2963–2967. [CrossRef]

38. Jayasayee, K.; Van Veen, J.R.; Manivasagam, T.G.; Celebi, S.; Hensen, E.J.; De Bruijn, F.A. Oxygen reduction reaction (ORR) activity and durability of carbon supported PtM (Co, Ni, Cu) alloys: Influence of particle size and non-noble metals. *Appl. Catal. B Environ.* **2012**, *111*, 515–526. [CrossRef]

39. Mani, P.; Srivastava, R.; Strasser, P. Dealloyed binary PtM3 (M= Cu, Co, Ni) and ternary PtNi3M (M= Cu, Co, Fe, Cr) electro-catalysts for the oxygen reduction reaction: Performance in polymer electrolyte membrane fuel cells. *J. Power Sources* **2011**, *196*, 666–673. [CrossRef]

40. Wang, C.; Waje, M.; Wang, X.; Tang, J.M.; Haddon, R.C.; Yan, Y. Proton exchange membrane fuel cells with carbon nanotube based electrodes. *Nano Lett.* **2004**, *4*, 345–348. [CrossRef]

41. Arico, A.; Shukla, A.; Kim, H.; Park, S.; Min, M.; Antonucci, V. An XPS study on oxidation states of Pt and its alloys with Co and Cr and its relevance to electroreduction of oxygen. *Appl. Surf. Sci.* **2001**, *172*, 33–40. [CrossRef]

42. Shukla, A.; Neergat, M.; Bera, P.; Jayaram, V.; Hegde, M. An XPS study on binary and ternary alloys of transition metals with platinized carbon and its bearing upon oxygen electroreduction in direct methanol fuel cells. *J. Electroanal. Chem.* **2001**, *504*, 111–119. [CrossRef]

43. Toda, T.; Igarashi, H.; Uchida, H.; Watanabe, M. Enhancement of the electroreduction of oxygen on Pt alloys with Fe, Ni, and Co. *J. Electrochem. Soc.* **1999**, *146*, 3750. [CrossRef]

44. Toda, T.; Igarashi, H.; Watanabe, M. Role of electronic property of Pt and Pt alloys on electrocatalytic reduction of oxygen. *J. Electrochem. Soc.* **1998**, *145*, 4185. [CrossRef]

45. Stamenković, V.; Schmidt, T.; Ross, P.; Marković, N. Surface composition effects in electrocatalysis: Kinetics of oxygen reduction on well-defined Pt3Ni and Pt3Co alloy surfaces. *J. Phys. Chem. B* **2002**, *106*, 11970–11979. [CrossRef]

46. Stamenkovic, V.R.; Fowler, B.; Mun, B.S.; Wang, G.; Ross, P.N.; Lucas, C.A.; Marković, N.M. Improved oxygen reduction activity on Pt3Ni (111) via increased surface site availability. *Science* **2007**, *315*, 493–497. [CrossRef] [PubMed]

47. Hoshi, Y.; Yoshida, T.; Nishikata, A.; Tsuru, T. Dissolution of Pt–M (M: Cu, Co, Ni, Fe) binary alloys in sulfuric acid solution. *Electrochim. Acta* **2011**, *56*, 5302–5309. [CrossRef]

48. Paulus, U.; Wokaun, A.; Scherer, G.; Schmidt, T.; Stamenkovic, V.; Markovic, N.M.; Ross, P. Oxygen reduction on high surface area Pt-based alloy catalysts in comparison to well defined smooth bulk alloy electrodes. *Electrochim. Acta* **2002**, *47*, 3787–3798. [CrossRef]

49. Huang, Q.; Yang, H.; Tang, Y.; Lu, T.; Akins, D.L. Carbon-supported Pt–Co alloy nanoparticles for oxygen reduction reaction. *Electrochem. Commun.* **2006**, *8*, 1220–1224. [CrossRef]

50. de Oliveira, J.B.; Guerrini, L.M.; Conejo, L.d.S.; Rezende, M.C.; Botelho, E.C. Viscoelastic evaluation of epoxy nanocomposite based on carbon nanofiber obtained from electrospinning processing. *Polym. Bull.* **2019**, *76*, 6063–6076. [CrossRef]

51. Mohamed, I.M.; Yasin, A.S.; Barakat, N.A.; Song, S.A.; Lee, H.E.; Kim, S.S. Electrocatalytic behavior of a nanocomposite of Ni/Pd supported by carbonized PVA nanofibers towards formic acid, ethanol and urea oxidation: A physicochemical and electro-analysis study. *Appl. Surf. Sci.* **2018**, *435*, 122–129. [CrossRef]

52. Shao, M.; Wang, D.; Yu, G.; Hu, B.; Yu, W.; Qian, Y. The synthesis of carbon nanotubes at low temperature via carbon suboxide disproportionation. *Carbon* **2004**, *42*, 183–185. [CrossRef]

53. Anwar, M.M.; Sheikh, F.A.; Kim, H. Comparative study of vapor pressure prediction methods for alcohol–gasoline blends. *Energy Environ. Focus* **2013**, *2*, 171–175. [CrossRef]

54. Singh, S.; Verma, N. Fabrication of Ni nanoparticles-dispersed carbon micro-nanofibers as the electrodes of a microbial fuel cell for bio-energy production. *Int. J. Hydrog. Energy* **2015**, *40*, 1145–1153. [CrossRef]

55. Mahanta, N.; Valiyaveettil, S. In situ preparation of silver nanoparticles on biocompatible methacrylated poly (vinyl alcohol) and cellulose based polymeric nanofibers. *RSC Adv.* **2012**, *2*, 11389–11396. [CrossRef]

56. Shi, W.; Ding, R.; Li, X.; Xu, Q.; Liu, E. Enhanced performance and electrocatalytic kinetics of Ni-Mo/graphene nanocatalysts towards alkaline urea oxidation reaction. *Electrochim. Acta* **2017**, *242*, 247–259. [CrossRef]

57. Singh, S.; Verma, N. Graphitic carbon micronanofibers asymmetrically dispersed with alumina-nickel nanoparticles: A novel electrode for mediatorless microbial fuel cells. *Int. J. Hydrog. Energy* **2015**, *40*, 5928–5938. [CrossRef]

58. Barakat, N.A.; Alajami, M.; Al Haj, Y.; Obaid, M.; Al-Meer, S. Enhanced onset potential NiMn-decorated activated carbon as effective and applicable anode in urea fuel cells. *Catal. Commun.* **2017**, *97*, 32–36. [CrossRef]

59. Raghuveer, V.; Manthiram, A.; Bard, A.J. Pd− Co− Mo electrocatalyst for the oxygen reduction reaction in proton exchange membrane fuel cells. *J. Phys. Chem. B* **2005**, *109*, 22909–22912. [CrossRef]

60. Nath, B.; Barbhuiya, T. Studies on the density and surface area of nanoparticles from Camellia sinensis, A natural source. *J. Chem. Pharm. Res* **2014**, *6*, 608–610.

61. Ballarin, B.; Seeber, R.; Tonelli, D.; Vaccari, A. Electrocatalytic properties of nickel (II) hydrotalcite-type anionic clay: Application to methanol and ethanol oxidation. *J. Electroanal. Chem.* **1999**, *463*, 123–127. [CrossRef]

62. García-Rodríguez, S.; Rojas, S.; Pena, M.; Fierro, J.; Baranton, S.; Léger, J. An FTIR study of Rh-PtSn/C catalysts for ethanol electrooxidation: Effect of surface composition. *Appl. Catal. B Environ.* **2011**, *106*, 520–528. [CrossRef]

63. Barakat, N.A.; Moustafa, H.M.; Nassar, M.; Abdelkareem, M.A.; Mahmoud, M.; Almajid, A.A.; Khalil, K.A. Distinct influence for carbon nano-morphology on the activity and optimum metal loading of Ni/C composite used for ethanol oxidation. *Electrochim. Acta* **2015**, *182*, 143–155. [CrossRef]

64. Wang, D.; Yan, W.; Vijapur, S.H.; Botte, G.G. Electrochemically reduced graphene oxide–nickel nanocomposites for urea electrolysis. *Electrochim. Acta* **2013**, *89*, 732–736. [CrossRef]

65. Ramachandran, K.; Babu, K.J. Ni-Co bimetal nanowires filled multiwalled carbon nanotubes for the highly sensitive and selective non-enzymatic glucose sensor applications. *Sci. Rep.* **2016**, *6*, 36583. [CrossRef] [PubMed]

66. Ma, X.; Ye, K.; Wang, G.; Duan, M.; Cheng, K.; Wang, G.; Cao, D. Facile fabrication of gold coated nickel nanoarrays and its excellent catalytic performance towards sodium borohydride electro-oxidation. *Appl. Surf. Sci.* **2017**, *414*, 353–360. [CrossRef]

67. Vedharathinam, V.; Botte, G.G. Understanding the electro-catalytic oxidation mechanism of urea on nickel electrodes in alkaline medium. *Electrochim. Acta* **2012**, *81*, 292–300. [CrossRef]

68. Kang, Y.; Wang, W.; Pu, Y.; Li, J.; Chai, D.; Lei, Z. An effective Pd-NiOx-P composite catalyst for glycerol electrooxidation: Co-existed phosphorus and nickel oxide to enhance performance of Pd. *Chem. Eng. J.* **2017**, *308*, 419–427. [CrossRef]

69. Sayed, E.T.; Eisa, T.; Mohamed, H.O.; Abdelkareem, M.A.; Allagui, A.; Alawadhi, H.; Chae, K.-J. Direct urea fuel cells: Challenges and opportunities. *J. Power Sources* **2019**, *417*, 159–175. [CrossRef]

70. Zhang, J.; Tse, Y.-H.; Pietro, W.J.; Lever, A. Electrocatalytic activity of N, N′, N″, N‴-tetramethyl-tetra-3, 4-pyridoporphyrazinocobalt (II) adsorbed on a graphite electrode towards the oxidation of hydrazine and hydroxylamine. *J. Electroanal. Chem.* **1996**, *406*, 203–211. [CrossRef]

71. AJ, M.; Machado, S.; Rabelo, F.; Santos, J., Jr. Electrochemical Study of Ethanol Oxidation on Nickel in. *J. Braz. Chem. Soc.* **1994**, *5*, 161–165.

72. Wang, W.; Chai, D.; Zhang, J.; Xue, S.; Wang, Y.; Lei, Z. Ni5Sm-P/C ternary alloyed catalyst as highly efficient electrocatalyst for urea electrooxidation. *J. Taiwan Inst. Chem. Eng.* **2017**, *80*, 326–332. [CrossRef]

73. Salamon, J.; Sathishkumar, Y.; Ramachandran, K.; Lee, Y.S.; Yoo, D.J.; Kim, A.R. One-pot synthesis of magnetite nanorods/graphene composites and its catalytic activity toward electrochemical detection of dopamine. *Biosens. Bioelectron.* **2015**, *64*, 269–276. [CrossRef] [PubMed]

74. Zayed, M.; Ahmed, A.M.; Shaban, M. Synthesis and characterization of nanoporous ZnO and Pt/ZnO thin films for dye degradation and water splitting applications. *Int. J. Hydrog. Energy* **2019**, *44*, 17630–17648. [CrossRef]

75. Shaban, M.; BinSabt, M.; Ahmed, A.M.; Mohamed, F. Recycling rusty iron with natural zeolite to create a unique nanocatalyst for green hydrogen production. *Nanomatererials* **2021**, *11*, 3445. [CrossRef]

76. Parsa, A.; Amanzadeh-Salout, S. Electrocatalytic activity and electrochemical impedance spectroscopy of poly (aniline-co-ortho-phenylenediamine) modified electrode on ascorbic acid. *Orient. J. Chem.* **2016**, *32*, 2051. [CrossRef]

77. Feng, L.-J.; Zhang, X.-H.; Zhao, D.-M.; Wang, S.-F. Electrochemical studies of bovine serum albumin immobilization onto the poly-o-phenylenediamine and carbon-coated nickel composite film and its interaction with papaverine. *Sens. Actuator B-Chem.* **2011**, *152*, 88–93. [CrossRef]

78. Shaban, M.; Kholidy, I.; Ahmed, G.M.; Negem, M.; El-Salam, H.M.A. Cyclic voltammetry growth and characterization of Sn–Ag alloys of different nanomorphologies and compositions for efficient hydrogen evolution in alkaline solutions. *RSC Adv.* **2019**, *9*, 22389–22400. [CrossRef]

79. Barakat, N.A.M.; Ali Abdelkareem, M.; Abdelghani, E.A.M. Influence of Sn Content, Nanostructural Morphology, and Synthesis Temperature on the Electrochemical Active Area of Ni-Sn/C Nanocomposite: Verification of Methanol and Urea Electrooxidation. *Catalysts* **2019**, *9*, 330. [CrossRef]

80. Gracita, M.; Tomboc, M.W.; Abebe, A.F.; Baye, H.K. Utilization of the superior properties of highly mesoporous PVP modified NiCo2O4 with accessible 3D nanostructure and flower-like morphology towards electrochemical methanol oxidation reaction. *J. Energy Chem.* **2019**, *29*, 136–146. [CrossRef]

81. Atbas, D.; Çağlar, A.; Kivrak, H.; Kivrak, A. Microwave Assisted Synthesis of Sn Promoted Pt Catalysts and Their Ethanol Electro-oxidation Activities. *Am. J. Nanomater.* **2016**, *4*, 8–11. [CrossRef]

82. Barakat, N.A.M.; Amen, M.T.; Al-Mubaddel, F.S.; Karim, M.R.; Alrashed, M. NiSn nanoparticle-incorporated carbon nanofibers as efficient electrocatalysts for urea oxidation and working anodes in direct urea fuel cells. *J. Adv. Res.* **2018**, *16*, 43–53. [CrossRef]

83. Amal, Z.; Waleed, M.A.; Rouby, W.M.E.; Barakat, N.A.M. Tungsten incorporation in nickel doped carbon nanofibers as efficient electrocatalyst for ethanol oxidation. *Fuel* **2020**, *280*, 118654. [CrossRef]